

Article

Study on Characteristics of Compression Deformation and Post-Peak Stress Rebound for Solid Waste Cemented Body

Xinyuan Zhao ¹, Ke Yang ^{2,*}, Xiang He ¹, Zhen Wei ¹, Jiqiang Zhang ¹ and Xiang Yu ¹

¹ State Key Laboratory of Mining Response and Disaster Prevention and Control in Deep Coal Mine, Anhui University of Science and Technology, Huainan 232001, China

² Institute of Energy, Hefei Comprehensive National Science Center, Hefei 230031, China

* Correspondence: keyang@aust.edu.cn

Abstract: Most of the previous studies focused on the mechanical characteristics before the stress peak of solid waste cemented backfill, but in the compression process of a solid waste cemented body, the phenomenon of post-peak stress rebound often occurs. Through the uniaxial compression experiment of a solid waste cemented body composed of coal gangue, fly ash, desulfurization gypsum, gasification slag, and furnace bottom slag, this paper analyzed the compression deformation characteristics of a solid waste cemented body with different mix proportions before and after the stress peak, established the stress–strain curve model of rebound stress in the rising and descending section after the stress peak, and revealed the reasons for the rebound stress and secondary unloading of the cemented body after the stress peak. The results showed that the maximum rebound stress accounts for 40%–80% of the compressive strength, and the changes in the two are positively correlated. The stress–strain curve model is a cubic function in the post-peak stress rising section and a quadratic rational function in the descending section. With the increase in the maximum compressive strength of the cemented body, its maximum rebound stress also increases, but its corresponding compressive strain generally shows a downward trend. There is a positive correlation between the rebound stress increment and strain increment of the cemented body. The change in the supporting structure and the evolution of the failure form of the cemented body before and after the maximum rebound stress indicate that the compression failure of the residual supporting structure caused by the main crack is the main reason for the rebound of the stress after the peak value of the cemented body to the complete unloading.

Keywords: solid waste cemented body; stress–strain model; post-peak deformation; stress rebound characteristics; failure characteristics; underground backfilling; solid waste disposal



Citation: Zhao, X.; Yang, K.; He, X.; Wei, Z.; Zhang, J.; Yu, X. Study on Characteristics of Compression Deformation and Post-Peak Stress Rebound for Solid Waste Cemented Body. *Minerals* **2023**, *13*, 108. <https://doi.org/10.3390/min13010108>

Academic Editor: Abbas Taheri

Received: 18 November 2022

Revised: 27 December 2022

Accepted: 3 January 2023

Published: 10 January 2023



Copyright: © 2023 by the authors. Licensee MDPI, Basel, Switzerland. This article is an open access article distributed under the terms and conditions of the Creative Commons Attribution (CC BY) license (<https://creativecommons.org/licenses/by/4.0/>).

1. Introduction

During the production and utilization of coal, a large number of solid wastes are generated, such as coal gangue, fly ash, and gasification slag [1,2]. If these solid wastes cannot be treated in a reasonable and effective way, they will cause serious pollution to the surface air, water, and soil, and even threaten the safety and health of the people [3,4]. Cemented backfill, as an underground green mining technology, has been rapidly developed and widely used in China in recent years [5–7]. Solid waste that meets environmental standards as cemented backfill materials in mines can not only be treated reasonably and effectively, but also has the advantages of green mining and has multiple effects [8,9].

The mechanical properties of the cemented backfill are key to the control effect of the underground surrounding rock and are also important content in the practical application of underground backfilling technology [10–12]. Many scholars have conducted a lot of research work on the mechanical properties of solid waste cemented backfill. For example, Fall et al. [13] studied the stress–strain behaviors of cemented paste backfill subjected to uniaxial compression and conventional triaxial tests, and discussed the effect of cemented

paste backfill basic components, strength, ageing, and confining pressure, on the deformation behavior of cemented paste backfill; Cavusoglu et al. [14] studied the effect of sodium silicate as an accelerator on the early mechanical and microstructure properties of cemented coal flash backfill; Yuuryun et al. [15,16] studied a backfill material based on industrial waste, which has necessary strength characteristics and transportability, and also activated the composite material composed of solid wastes to improve its strength characteristics; Zhao et al. [17] carried out a study on the cooperative deformation characteristics of two combinations with different lime–sand ratios by means of uniaxial compression tests; Wang et al. [18] used CT to study the stress–strain response and microstructure changes of cemented waste rock backfill under uniaxial compression; Liu et al. [19] studied the compressive strength and deformation law of loess waste rock cemented backfill; Guo et al. [20] studied the deformation and instability characteristics of gangue cemented backfill in the process of advancing the working face; Wu et al. [21] analyzed the influence of the Talbol power exponent, initial porosity, and type and content of cementing material on the strength and deformation characteristics of waste rock cemented backfill; Wang et al. [22] studied the failure mode, crack evolution, and damage constitutive relationship of the layered colloidal tailings backfill by the uniaxial compression test; Tu et al. [23] established the compressive constitutive model of cemented tailing backfill and analyzed the failure mode of backfill under uniaxial compression; Yang et al. [24] studied the stress–strain response, failure mode, and criterion of cemented tailings backfill under a triaxial compression load with different confining pressures and components through experiments; Ermolovich et al. [25] studied a composite based on waste from the processing of water-soluble ores, and used additives to improve the strength characteristics of the material and analyzed its microstructure. Many other scholars have studied the properties and deformation characteristics of solid waste materials [26–28]. Analyzing the above, it can be noted that solid waste backfill material is a very topical issue. Most of the backfill materials used in previous studies are single or two kinds of solid wastes, such as coal gangue, tailings, and fly ash, and few of them are multi-source solid wastes generated by coal mines, thermal power plants, and the coal chemical industry. The use of multi-source solid waste for underground backfilling can effectively and cost-effectively dispose of solid waste. In addition, in the process of compression deformation of a solid waste cemented body, the phenomena of stress rebound and secondary unloading occur after the stress reaches the peak value for the first time. The previous studies on the mechanical properties of the solid waste cemented body mostly focused on the pre-peak stress and strain characteristics, and less on the post-peak deformation characteristics of the cemented body. It is helpful to understand the mechanism of controlling the roof and reducing the subsidence of cemented backfill by studying the post-peak deformation characteristics of cemented backfill.

This paper analyzes the compressive strength and residual strength of solid waste cemented backfill, establishes the post-peak stress–strain curve model, studies the post-peak deformation characteristics of the cemented backfill by using the relationship between the maximum rebound stress and the maximum compressive strength, compression strain, and other parameters, and finally analyzes the support structure changes and failure morphology evolution characteristics of the specimen before and after the maximum rebound stress, revealing the reasons for the post-peak stress rebound and instability of the cemented backfill. It is of great significance to study the stress rebound characteristics of solid waste cemented backfill for improving the safety of backfill in controlling the surrounding rock.

2. Experiment Design

2.1. Experimental Material

The cemented body is mainly composed of five Class I solid waste materials, namely coal gangue, fly ash, desulfurization gypsum, gasification slag, and furnace bottom slag, plus a small amount of cement. The experimental materials are shown in Figure 1.



Figure 1. Experimental materials.

The coal gangue comes from a coal mine in Ningxia, China. The original gangue is screened after crushing. The gangue with a particle size of less than 15 mm is used as the experimental material. The fly ash is secondary fly ash with a fineness of 20 and loss on ignition of 3.5%. The grain size of fly ash used in this experiment is basically 0.15–200 μm . The particle size of the furnace bottom slag and gasification slag in the experiment is less than 2.5 mm. The cement used in this experiment is Hailuo cement produced by Huainan Cement Plant, with the grade of P. O 32.5, fineness of 20, specific surface area of 343 m^2/g , and density of 3.1 g/cm^3 .

A Bruker D8 Advance is used to test the solid waste materials. The test method refers to the XRD test method in reference [25]. The scanning angle is 5–70° and the speed is 5°/min. JADE software and the PDF card are used to analyze the test results. The XRD results of desulfurization gypsum, furnace bottom slag, and gasification slag are shown in Figure 2. The main mineral components of furnace bottom slag are quartz and mullite, and a small amount of hematite; the main mineral components of gasification slag are quartz; the main components of desulfurization gypsum are dihydrate gypsum.

The composition test and analysis of the solid waste materials used in the experiment are shown in Table 1.

It can be found that the main oxide components of coal gangue are SiO_2 , CO_2 , Al_2O_3 , Fe_2O_3 , etc. The main oxide components of fly ash are SiO_2 , CO_2 , Al_2O_3 , Fe_2O_3 , CaO , etc. The main oxide components of desulfurization gypsum are CO_2 , SO_3 , CaO , SiO_2 , MgO , etc. The largest oxide component of gasification slag is CO_2 , accounting for more than 77%, followed by SiO_2 , Al_2O_3 , Fe_2O_3 , CaO , etc. The main oxide components of furnace bottom slag are SiO_2 , CO_2 , Al_2O_3 , Fe_2O_3 , and CaO .

2.2. Experimental Program

There is much literature on the mechanical properties of backfill materials composed of gangue, fly ash, and cement [29–31]. Therefore, in this experiment, the six backfill materials are made into a new solid waste cemented body by adding different amounts of desulfurization gypsum, gasification slag, and furnace bottom slag on the basis of gangue, fly ash, and cement. To fully study the post-peak deformation and failure characteristics of the solid waste cemented body, five groups of experiments are designed to make cemented specimens. Each group of experiments is designed with three ages, and three specimens are prepared at each age. The specimens with the strength closest to the average strength are selected for analysis. The material ratio in each experimental group is shown in Table 2. The dosage of desulfurization gypsum, furnace bottom slag, and gasification slag is randomly matched within a certain range. The material mixing, specimen demolding, curing, and compression testing of the cemented body specimens are made according to the

Chinese standard “Standard for Test Methods of Properties of Ordinary Concrete Mixes” (GB/T50080-2016): First, prepare the solid waste materials in proportion, mix the prepared solid materials, and add water in the mixer for mixing for more than 2 min until they are evenly mixed. Then, fill the test mold with evenly mixed backfill materials in turn. The test mold is a cube mold with a length, width, and height of 70.7 mm. The curing conditions of the specimens are $25 \pm 2 \text{ }^\circ\text{C}$ and 80% relative humidity. Because the early mechanical properties of the cemented backfill play a key role in the control of the rock strata, and the research on the early properties of the cemented backfill is very important in the research of modern underground backfilling technology, the curing time of the cemented body is set as 1 d, 3 d, and 7 d in this experiment. After the specimens are cured for a corresponding time, a microcomputer-controlled servo press is used to carry out uniaxial compression tests. The loading speed is 0.01 kN/s and the specimen is continuously loaded until it is completely destroyed.

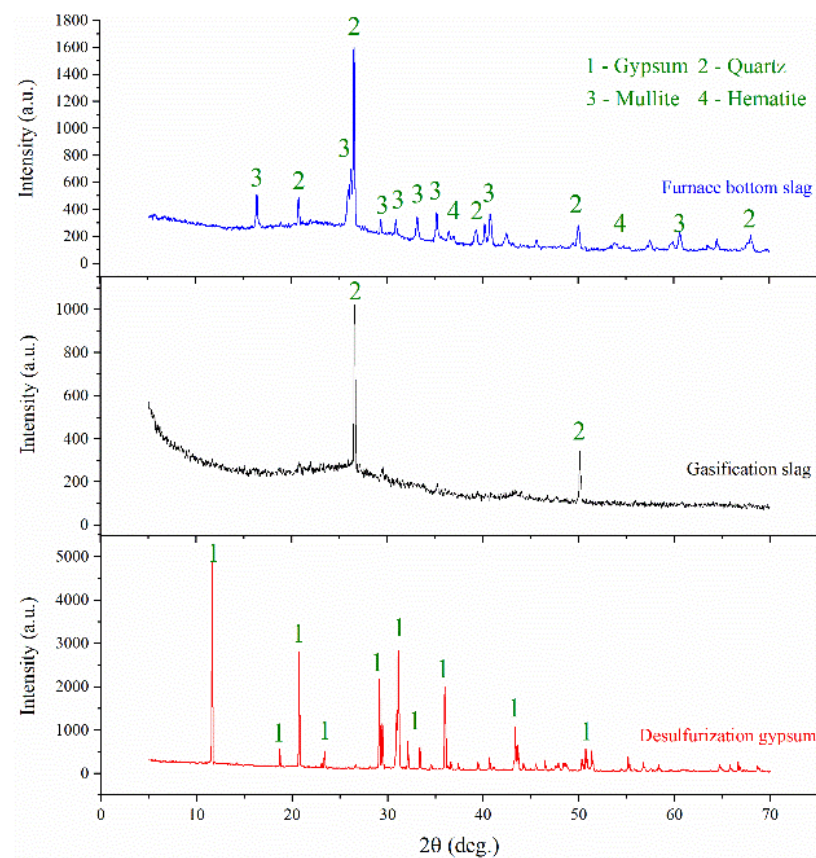


Figure 2. Particle size distribution of three solid wastes.

Table 1. XRF results of solid waste materials.

Coal Gangue		Fly Ash		Desulfurization Gypsum		Gasification Slag		Furnace Bottom Slag	
Oxides	Content/%	Oxides	Content/%	Oxides	Content/%	Oxides	Content/%	Oxides	Content/%
SiO ₂	43.61	SiO ₂	40.4	CO ₂	38.2	SiO ₂	10.4	CO ₂	73
CO ₂	26.1	CO ₂	23.9	SO ₃	32.76	CO ₂	77.5	SiO ₂	15.75
Al ₂ O ₃	20.9	Al ₂ O ₃	19	CaO	23.36	Al ₂ O ₃	2.61	Al ₂ O ₃	3.77
Fe ₂ O ₃	3.352	Fe ₂ O ₃	5.102	SiO ₂	2.26	CaO	3.51	Fe ₂ O ₃	3.264
K ₂ O	2.26	CaO	4.28	MgO	1.3	Fe ₂ O ₃	3.09	CaO	2.26
Others	3.778	Others	7.318	Others	2.12	Others	2.89	Others	1.956

Table 2. Preparation ratio of cemented specimen.

Experiment No.	Gangue/kg	Fly Ash/kg	Cement/kg	Desulfurized Gypsum/kg	Furnace Bottom Slag/kg	Gasification Slag/kg	Mass Fraction
A	1	0.4	0.1	0.30	0.20	0.10	80%
B				0.40	0.20	0.20	
C				0.20	0.15	0.10	
D				0.30	0.15	0.20	
E				0.30	0.10	0.30	

3. Experimental Results

3.1. Compression Deformation Characteristics

The stress–strain curves of cemented specimens in each experimental group at different curing ages are obtained by compression test, as shown in Figure 3.

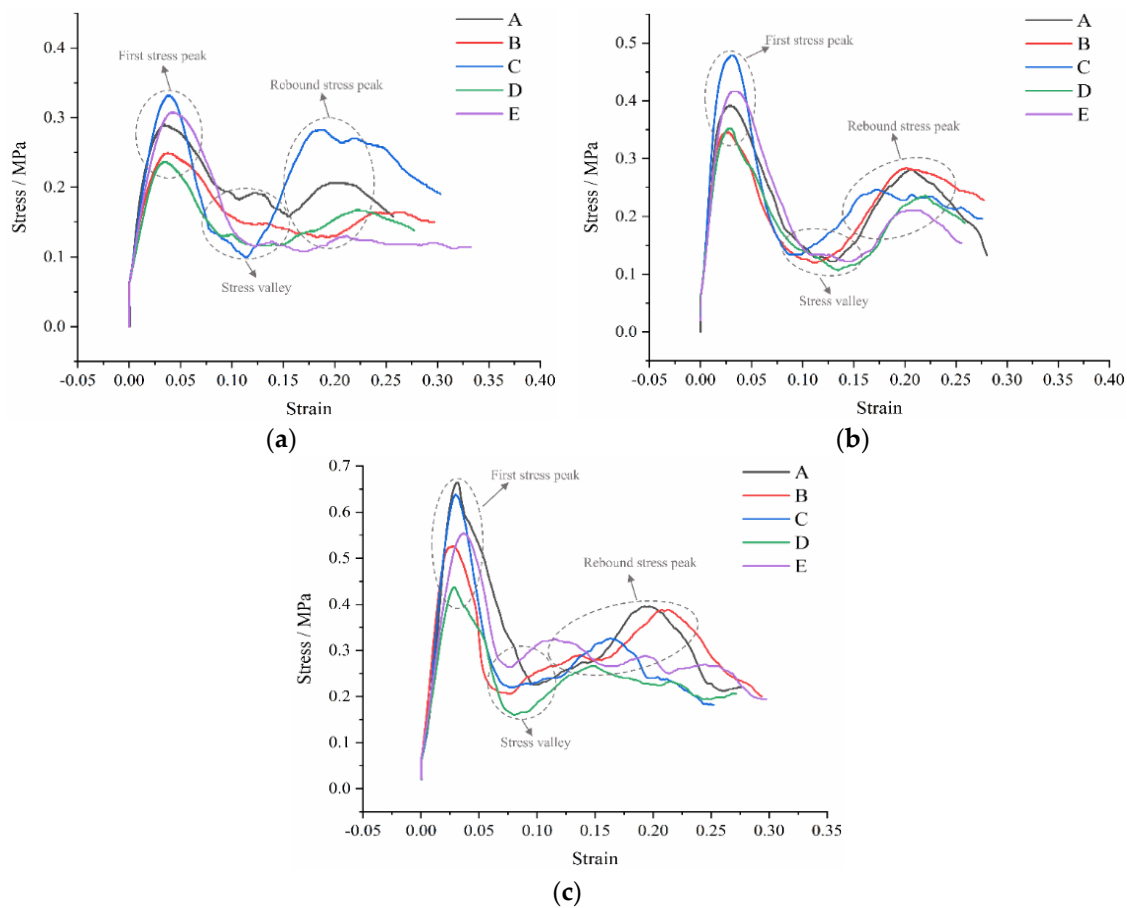


Figure 3. Stress–strain curves of cemented specimens at different curing ages: (a) 1 d, (b) 3 d, and (c) 7 d.

It can be seen from Figure 3a–c that the compression stress–strain curves of the cemented specimens in different experimental groups at different curing ages are basically similar, showing a bimodal shape. The stress borne by the specimens has experienced two peaks in the compression process, namely the first stress peak and rebound stress peak. The first stress peak and the rebound stress peak represent the maximum compressive strength and the maximum rebound stress, respectively, so the maximum compressive strength is obviously higher than the maximum rebound stress. After the upper indenter of the testing machine touches the specimen, the compressive stress on the specimen starts to increase rapidly, and the compressive strain increases slowly. When the stress reaches the maximum compressive strength, multiple cracks appear on the surface of the specimen,

and the compressive strain of the specimen is generally small at this time, basically located between 0.03 and 0.05. After that, the stress on the specimen decreases rapidly, and the compressive strain also starts to increase rapidly. When the stress drops to between 0.1 MPa and 0.2 MPa, the downward trend of stress stops and begins to oscillate briefly to form a stress valley shape, and then the stress begins to rise slowly. At this time, the compressive strain of the specimen continues to increase. As the compressive strain of the specimen continues to increase, the internal residual support structure is further destroyed, and the stress reaches the maximum rebound stress and then slowly decreases, at which time a rebound stress peak is formed.

The maximum strength and valley values of the cemented specimens in each experimental group at different curing ages are very different. When the curing age is 1 d, the maximum compressive strength and maximum rebound stress of the cemented specimen in experimental group C are largest, but its stress valley is smallest. The maximum compressive strength of the cemented specimen in experimental group D is smallest, the maximum rebound stress is smallest in experimental group E, and the stress valley in experimental group A is largest. When the curing age is 3 d, the maximum compressive strength and stress valley value of the cemented specimen in experimental group C are largest, and the maximum rebound stress of the cemented specimen in experimental group B is largest, but its maximum compressive strength is smallest. The maximum rebound stress in experimental group E is smallest, and the stress valley value of the specimen in experimental group D is smallest. When the curing age is 7 d, the maximum compressive strength and maximum rebound stress of the cemented specimen in experimental group A are largest; the maximum compressive strength, stress valley value, and maximum rebound stress of the cemented specimen in experimental group D are smallest; the stress valley value of the cemented specimen in experimental group E is largest.

According to the relationship between the elastic modulus of the specimen and its curing time (Figure 4), when the curing time is 1 d, the elastic modulus of the specimen is generally smallest, indicating that the strength of the specimen is low and large deformation occurs under a small pressure. The elastic modulus of the cement cured for 3 days and 7 days has little difference.

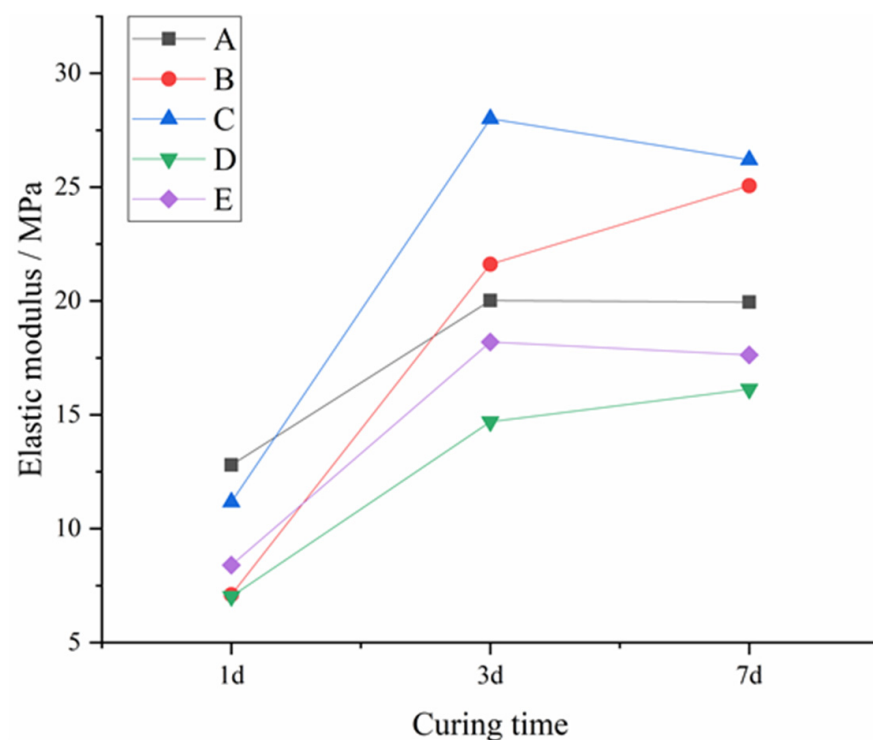


Figure 4. The elastic modulus of the specimen at different curing times.

3.2. Strength Characteristics

To analyze the variation law of the maximum compressive strength and maximum rebound stress of the cemented specimen at different curing ages, the stress peak data of the cemented specimen are extracted and the curve is drawn, as shown in Figure 5a,b.

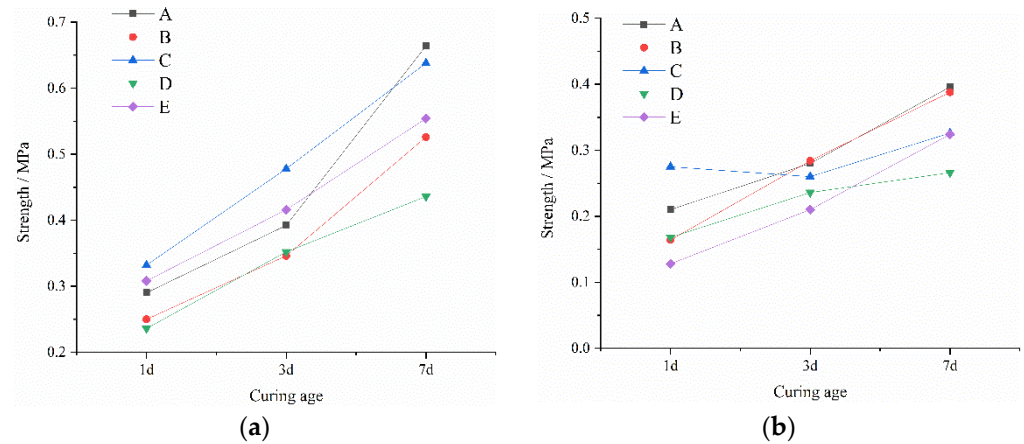


Figure 5. Two stress peaks of specimens: (a) maximum compressive strength; (b) maximum rebound stress.

Figure 5a shows the variation law of the maximum compressive strength of the cemented specimens in different experimental groups at different curing ages, which illustrates the relationship between the compressive strength of the cemented specimens and the curing ages. It is obvious that the early strength of cemented samples in each specimen is positively related to the curing age when the curing age is less than 7 d. The compressive strength of the cemented specimens reaches the maximum when the curing age is 7 d, and the specimen with the maximum strength at 7 d is the specimen of experimental group A, with a strength of about 0.68 MPa. The strength increase values of cemented specimens in each experimental group from 1 d to 7 d are A: 0.36 MPa, B: 0.28 MPa, C: 0.31 MPa, D: 0.2 MPa, and E: 0.25 MPa, and the strength increase value of experimental group A is largest.

Figure 5b shows the variation law of the maximum rebound stress of the cemented specimens in the same experimental group at different curing ages. It can be found that the maximum rebound stress of cemented specimens in different experimental groups generally shows a change law that gradually increases with the increase in curing age, which is basically consistent with the variation law of the maximum compressive strength. The increased value of the maximum rebound stress of the cemented specimen in experimental group B is largest from 1 d to 7 d, which is 0.24 MPa. This indicates that the maximum rebound stress of the cemented specimens in experimental group B has the largest variation before 7 d. The maximum rebound stress of the cemented specimen in experimental group C at the curing age of 3 d decreases compared with 1 d, but the decrease range is very small.

It can be seen from the change rule of compressive strength and maximum rebound stress that the cemented body has not been completely destroyed after reaching the ultimate compressive strength, and there is a residual supporting structure. The compressive strength of the cemented body affects the supporting performance of the residual structure, and the strength of the residual supporting structure determines the rebound degree of the post-peak stress.

3.3. The Relationship between Maximum Rebound Stress and Compressive Strength

To analyze the relationship between the maximum rebound stress and the compressive strength, a scatter plot is drawn and fitted with a trend line, as shown in Figure 6.

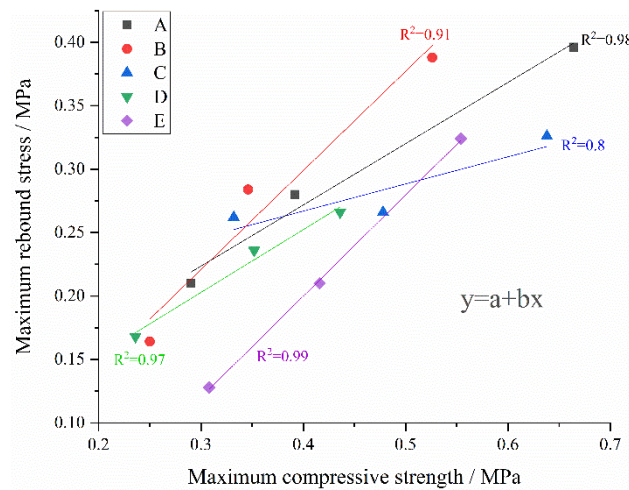


Figure 6. Relationship between maximum compressive strength and maximum rebound stress.

It can be seen from Figure 6 that the fitting curve formulas of the maximum compressive strength and maximum rebound stress of the cement specimen are $y = a + bx$, and the relationship between the maximum compressive strength and the maximum rebound stress of the cemented specimen is positively correlated; that is, with the increase in the maximum compressive strength, the maximum rebound stress also shows an increasing trend, indicating that the higher the maximum compressive strength of the cemented specimen, the higher the maximum rebound stress. The maximum compressive strength of the cemented specimen in each experimental group is between 0.2 and 0.7 MPa, and the maximum rebound stress is between 0.1 and 0.4 MPa. According to the slope and length of the fitting line, the fitting line slope of the cemented specimen in experimental group B is largest, which shows that the change range of the maximum rebound stress of the cemented specimen in experimental group B at different curing ages is largest, while the change range of the maximum compressive strength is relatively small. The fitting line length of the cemented specimen in experimental group A is largest, indicating that the change range of the maximum compressive strength of the cemented specimen in experimental group A at different curing ages is largest.

The percentage of the maximum rebound stress to the maximum compressive strength is calculated, as shown in Table 3. It can be found that the maximum rebound stress of the cemented specimens is generally about 40%–80% of the maximum compressive strength, the maximum percentage is 84.94% for the specimens with a curing age of 1 d in experimental group C, and the minimum is 42% for the cemented specimens with a curing age of 1 d in experimental group E.

Table 3. Percentage of maximum rebound stress to maximum compressive strength.

No.	Curing Age		
	1 d	3 d	7 d
A	72.41%	71.43%	59.64%
B	65.6%	82.08%	73.76%
C	84.94%	52%	51.1%
D	71.19%	67.05%	61.01%
E	42%	50%	58%

3.4. Rebound Stress Curve Model

From the above analysis, it can be seen that the stress–strain compression curves of the cemented specimens in each experimental group at different curing ages are generally similar, so the stress–strain curve model of the cemented specimens is constructed, as shown in Figure 7.

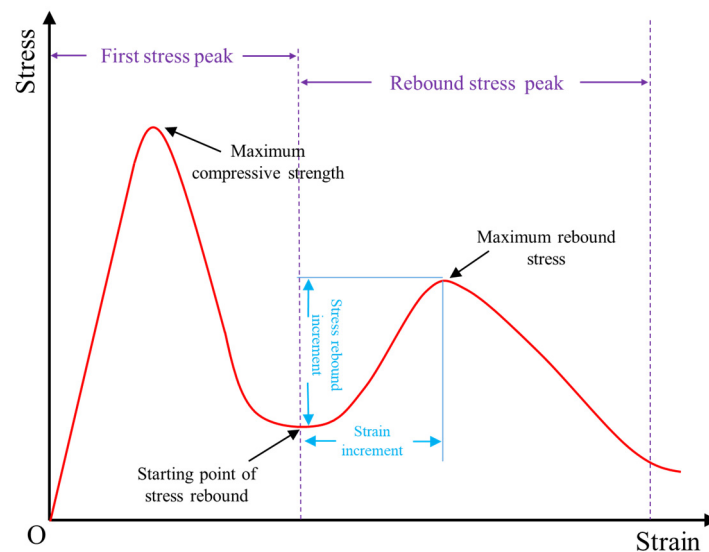


Figure 7. Stress–strain curve model.

The stress on the cemented specimen experiences two peaks in the compression process, namely, the first stress peak and the rebound stress peak. The first stress peak is the stress–strain curve of the specimen in the conventional uniaxial compression experiment, but the rebound stress peak curve is rare. In the first stress peak curve, the rational fraction function can better fit the compression curve. Referring to the complete stress–strain curve equation of concrete under uniaxial compression [32,33], in the rising section of the stress curve, the stress–strain relationship is Equation (1):

$$\frac{\sigma}{f_c} = \alpha_a \left(\frac{\epsilon}{\epsilon_p}\right) + \alpha_b \left(\frac{\epsilon}{\epsilon_p}\right)^2 + \alpha_c \left(\frac{\epsilon}{\epsilon_p}\right)^3 \tag{1}$$

In the descending section of the stress curve, the stress–strain relationship is Equation (2):

$$\frac{\sigma}{f_c} = \frac{\alpha_d \left(\frac{\epsilon}{\epsilon_p}\right)}{\alpha_e \left(\left(\frac{\epsilon}{\epsilon_p}\right) - 1\right)^2 + \alpha_f \left(\frac{\epsilon}{\epsilon_p}\right)} \tag{2}$$

where $\alpha_a, \alpha_b, \alpha_c, \alpha_d, \alpha_e,$ and α_f are the empirical parameters; ϵ and ϵ_p are the strain value and the strain value at the maximum stress, respectively; σ is the stress value; f_c is the maximum compressive strength.

In the stress rebound stage, the shape of the rebound stress peak curve is similar to that of the first stress peak curve. The turning point of the post-peak stress decline and rise is defined as the starting point of the stress rebound. Thus, in the rising section of the rebound stress curve, there is:

$$\frac{\sigma_r - \sigma_v}{f_r - \sigma_v} = \alpha_{ar} \left(\frac{\epsilon_r - \epsilon_v}{\epsilon_{rp} - \epsilon_v}\right) + \alpha_{br} \left(\frac{\epsilon_r - \epsilon_v}{\epsilon_{rp} - \epsilon_v}\right)^2 + \alpha_{cr} \left(\frac{\epsilon_r - \epsilon_v}{\epsilon_{rp} - \epsilon_v}\right)^3 \tag{3}$$

In the descending section of the rebound stress curve, the stress–strain relationship is as follows:

$$\frac{\sigma_r - \sigma_v}{f_r - \sigma_v} = \frac{\alpha_{dr} \left(\frac{\epsilon_r - \epsilon_v}{\epsilon_{rp} - \epsilon_v}\right)}{\alpha_{er} \left(\left(\frac{\epsilon_r - \epsilon_v}{\epsilon_{rp} - \epsilon_v}\right) - 1\right)^2 + \alpha_{fr} \left(\frac{\epsilon_r - \epsilon_v}{\epsilon_{rp} - \epsilon_v}\right)} \tag{4}$$

where $\alpha_{ar}, \alpha_{br}, \alpha_{cr}, \alpha_{dr}, \alpha_{er},$ and α_{fr} are the empirical parameters; σ_r and ϵ_r are the rebound stress and strain values, respectively; σ_v and ϵ_v are the stress and strain values at the starting point of the rebound stress rise, respectively; f_r is the maximum value of stress; ϵ_{rp} is the corresponding strain when the stress rebound reaches the maximum value.

In order to verify the applicability of the stress–strain equation in the rising and descending stages of the rebound stress curve to the rebound stress curve in this experiment, $y = \frac{\sigma_r - \sigma_v}{f_r - \sigma_v}$ and $x = \frac{\epsilon_r - \epsilon_v}{\epsilon_{rp} - \epsilon_v}$ are set, the stress rebound stress–strain curves of the specimen with a curing age of 3 d are taken as an example, the rebound stress peak curve is drawn and fitted, and the results are shown in Figure 8.

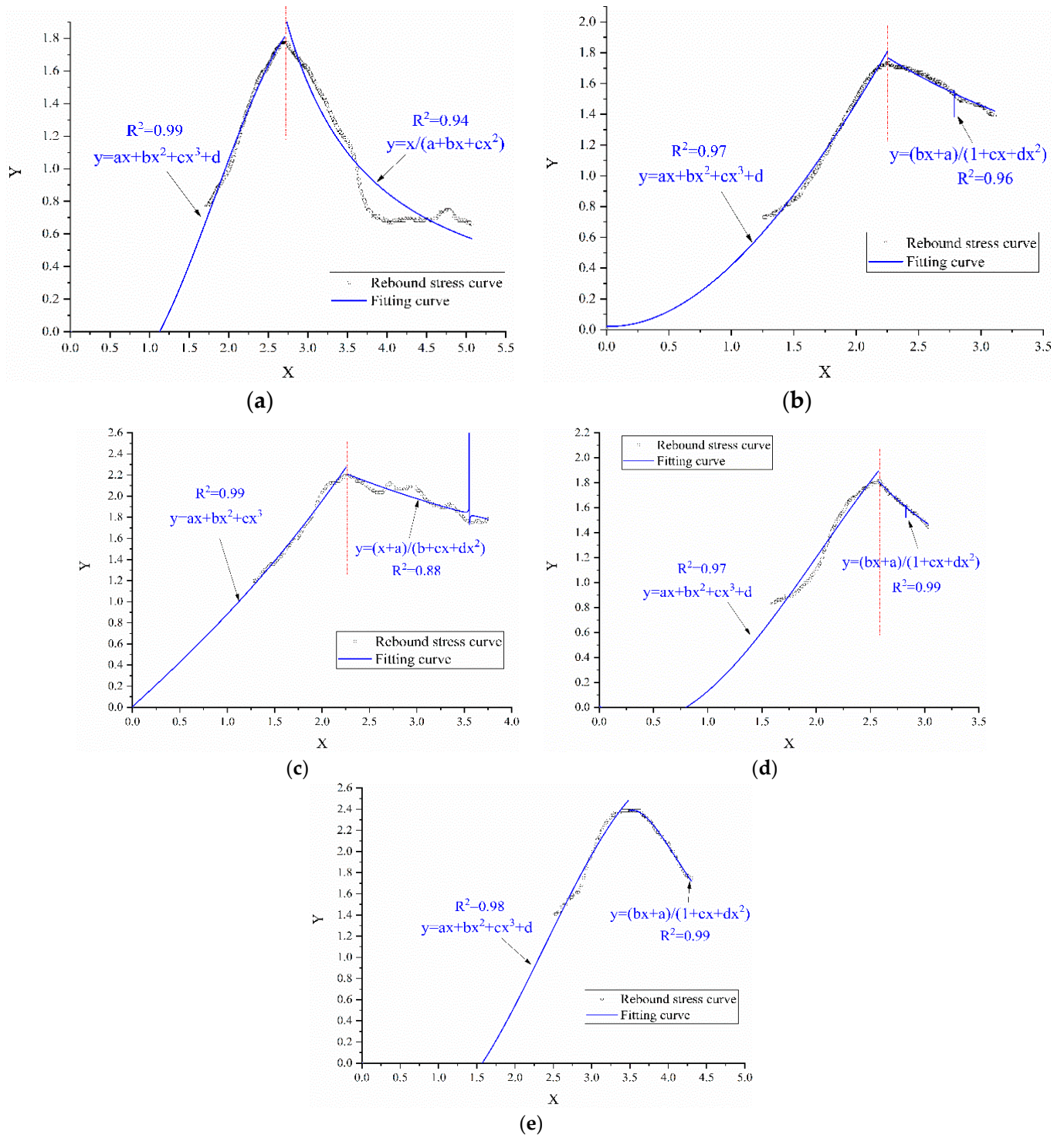


Figure 8. Fitting model of rebound stress curve of specimens in different experimental groups when the curing age is 3 d: (a) experimental group A, (b) experimental group B, (c) experimental group C, (d) experimental group D, and (e) experimental group E.

The fitting curve formulas of the rising section and the descending section listed in Figure 8a–e are shown in Table 4.

Table 4. The fitting curve formula of the stress rebound stage.

Experiment No.	Rising Section	Descending Section	Remark
A	$y = ax - bx^2 + cx^3 + d$ $R^2 = 0.99$	$y = \frac{x}{a+bx+cx^2}$ $R^2 = 0.94$	a, b, c, d are constants respectively
B	$y = ax + bx^2 + cx^3 + d$ $R^2 = 0.97$	$y = \frac{bx+a}{1+cx+dx^2}$ $R^2 = 0.96$	
C	$y = ax + bx^2 + cx^3$ $R^2 = 0.97$	$y = \frac{x+a}{b+cx+dx^2}$ $R^2 = 0.88$	
D	$y = ax + bx^2 + cx^3 + d$ $R^2 = 0.97$	$y = \frac{bx+a}{1+cx+dx^2}$ $R^2 = 0.99$	
E	$y = ax + bx^2 + cx^3 + d$ $R^2 = 0.98$	$y = \frac{bx+a}{1+cx+dx^2}$ $R^2 = 0.99$	

It can be seen from Table 3 that in the rising stage of the stress rebound curve, the fitting degree of the fitted curve is relatively high, and the correlation coefficient R^2 is all greater than 0.97. The basic form of the fitting formula is:

$$y = ax + bx^2 + cx^3 + d \quad (5)$$

Equation (5) is consistent with Equation (3) in function form, indicating that Equation (3) is applicable to the rising section curve model in the stress rebound peak of cemented body.

As shown in Figure 8a–e, by fitting the curve of the rising section in the rebound stress peak, the fitting formula of the rising section in the rebound stress peak is obtained, as shown in Equation (5), and the correlation coefficient R^2 is greater than 0.97, indicating a high fitting degree.

The fitting formula of the descending section in the rebound stress peak is as shown in Equation (6), the basic form of the curve fitting formula is Equation (6), and the correlation coefficient R^2 is greater than 0.88, indicating that the fitting degree is also high.

$$y = \frac{a_r + b_r x}{c_r + d_r x + e_r x^2} \quad (6)$$

Equation (6) is consistent with Equation (4) in function form, indicating that Equation (4) is also applicable in this experiment.

To sum up, the curve models of the rising and descending section in the stress rebound peak of the cemented body are Equations (3) and (4), respectively.

3.5. Stress–Strain Relationship in the Rebound Stage

In order to study the stress–strain relationship in the rebound stage, the maximum rebound stress and corresponding compressive strain, rebound stress increment, and strain increment are used as post-peak deformation parameters to analyze the variation relationship between them, as shown in Figure 9a,b. In the figures, the changing trend of each group of data is analyzed by linear fitting. The fitting equation is $y = a + bx$.

Figure 9a,b show that the correlation coefficient R^2 of the linear fitting equation is greater than 0.7, indicating a high degree of linear fitting. As can be seen from Figure 9a, the maximum rebound stress of the cemented specimen is negatively correlated with the corresponding compressive strain, that is, with the increase in the maximum rebound stress, the compressive strain of the specimen shows a downward trend in varying degrees, indicating that the higher the maximum rebound stress is, the smaller the compressive strain is. The maximum rebound stress of cemented specimens in each experimental group is between 0.1 and 0.4 MPa, and the compressive strain is between 0.1 and 0.25. The inclination degree of the fitting line represents the variation range of compressive strain when the rebound stress reaches the maximum rebound stress of the cemented specimens at different curing ages. The fitting line trend of the cemented specimen in experimental group D is steepest, and the fitting line trend of the cemented specimen in experimental

group B is the most gentle, indicating that the compressive strain of the cemented specimen in experimental group D with different curing ages changes the most at the maximum rebound stress, and that of the cemented specimen in experimental group B is smallest.

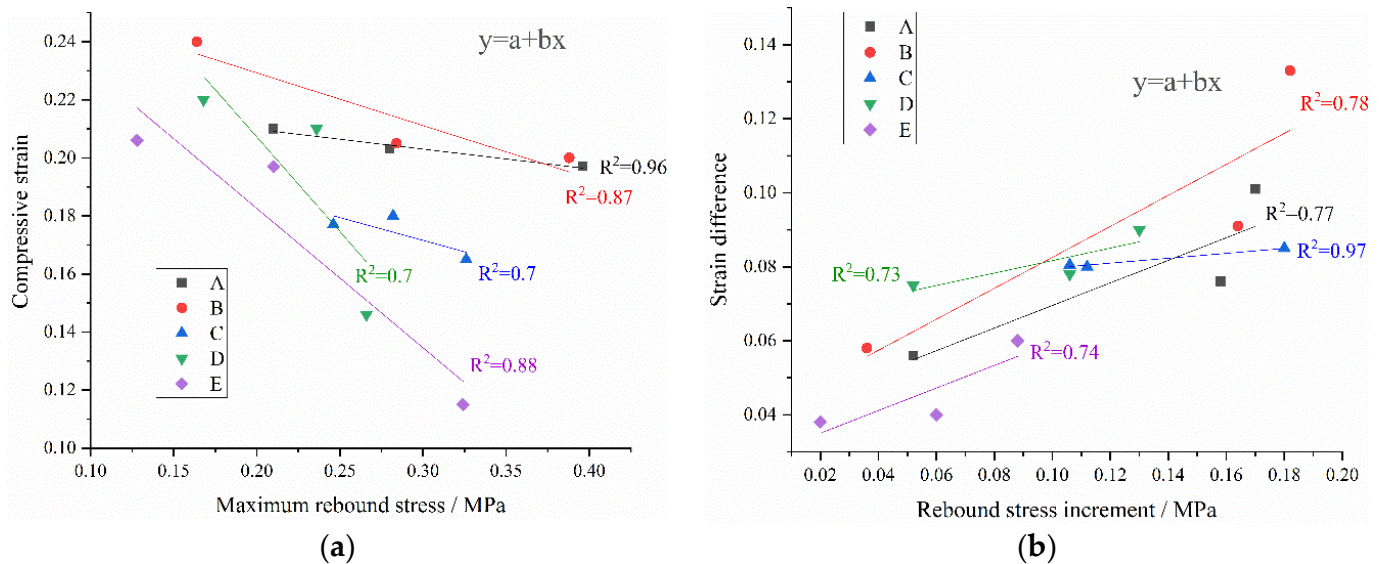


Figure 9. Post-peak deformation parameters: (a) maximum rebound stress and compressive strain; (b) rebound stress increment and strain difference.

It can be seen from Figure 9b that the rebound stress increment of the cemented specimen is positively correlated with the strain increment; that is, with the increase in the rebound stress increment, the strain increment also shows an increasing trend in varying degrees, indicating that in the residual support stage, the greater the rebound stress increment, the greater the compressive strain of the specimen. The rebound stress increment of the cemented specimens in each experimental group is generally between 0.02 and 0.19 MPa, and the strain increment is between 0.04 and 0.14. The fitting line of the cemented specimen in experimental group C has the lowest inclination, an almost horizontal trend, and the shortest length, indicating that the variation range of the rebound stress increment and strain increment of cemented specimens in experimental group C is smallest, ranging from 0.1 to 0.18 MPa and 0.078 to 0.08, respectively. The fitting line inclination of the cemented specimen in experimental group E is largest, indicating that the variation range of the strain increment is large and the variation range of the rebound stress increment is small, so the ratio of the two is largest. The fitting line length of the cemented specimen in experimental group B is largest, indicating that the variation range of the rebound stress increment is largest, which is between 0.04 and 0.19 MPa, and the variation range of the strain increment is relatively small.

3.6. Post-Peak Failure Characteristics

The cemented specimens of experimental groups A and D with a curing age of 7 days are taken as an example, and the compression failure characteristics of the specimen in the stress rebound stage are studied. The compression deformation process of the specimen before and after the maximum rebound stress is photographed, respectively, as shown in Figures 10 and 11.

It can be seen from Figure 10a that after the maximum compressive strength and before the maximum rebound stress, the whole specimen has been damaged, but there is still a large residual support structure. At this stage, a large number of blocks are peeled off and scattered around the specimen, the fracture line formed by the peeling of large blocks appears on the right side of the specimen, and there are multiple concave surfaces formed by the peeling of blocks on the upper part of the residual support structure. Although the

specimen has large compression deformation and expansion, its residual support structure still has a certain residual strength and bears a certain stress in the process of structural change and reconstruction. After the stress rebounds slowly to the peak value (Figure 10b), the specimen is further compressed and deformed, and the fracture line on the right side of the specimen is further expanded. A penetrating crack is derived from the middle and upper part of the fracture line, which divides the residual support structure into multiple small block structures. Larger blocks are tilted and staggered during compression, the concave surface at the upper part of the surface of the residual support structure is squeezed, and an unstable block appears at the upper corner. The main crack appears in the middle and lower part of the specimen, which penetrates the residual structure, the residual supporting structure is deeply damaged, the specimen loses the residual strength, and the rebound stress decreases slowly.

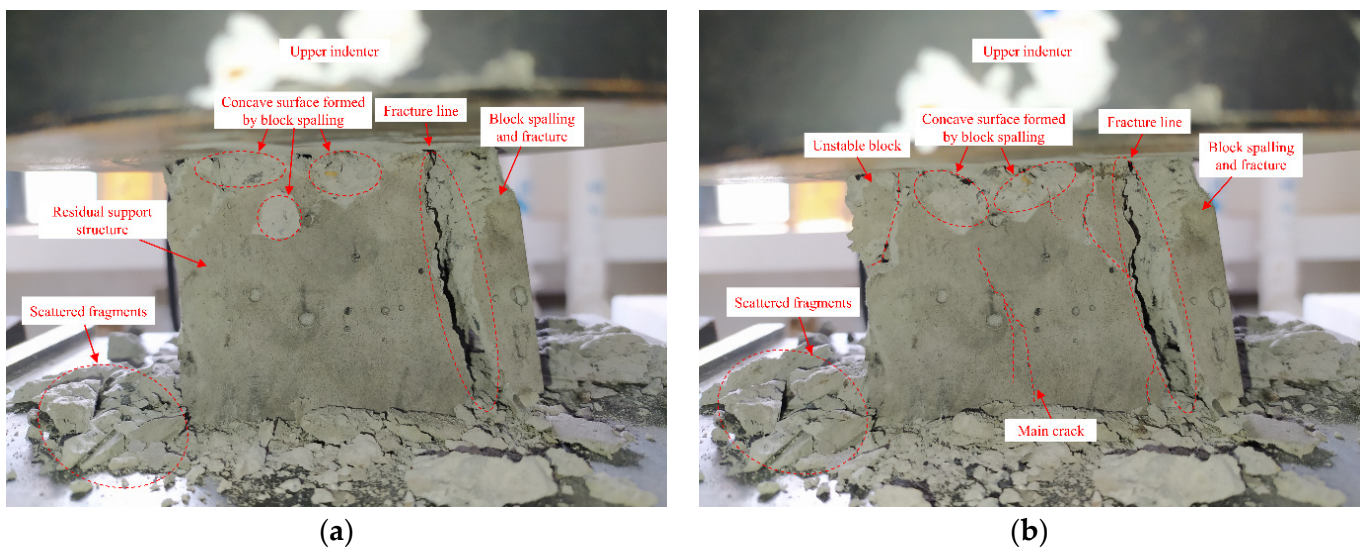


Figure 10. Failure morphology of specimens in experimental group A: (a) before the maximum rebound stress; (b) after the maximum rebound stress.

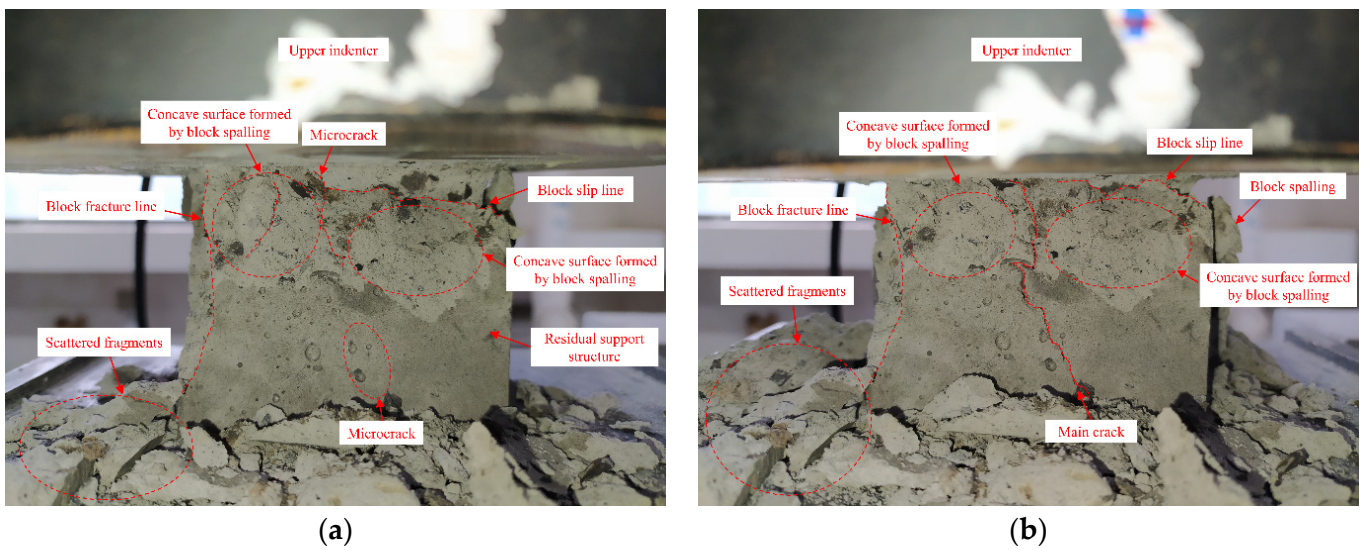


Figure 11. Failure morphology of specimens in experimental group D: (a) before the maximum rebound stress; (b) after the maximum rebound stress.

The failure evolution process of the cemented specimen in experimental group D before and after the maximum rebound stress is similar to that in experimental group A, as shown in Figure 11. In the stress rebound stage (Figure 11a), the upper part of the specimen is seriously damaged, the block is peeled off more, the concave surface is large, and there are several microcracks in the concave surface. There is a slip line formed by the slip dislocation of the upper block in the depth of the concave surface, which leads to the continuous increase in compressive strain. The left edge block peels off to form a fracture line. The middle and lower part of the specimen is a residual support structure, which has not been damaged in a large area. As the upper block slides downward, the specimen continues to undergo compression deformation, the residual support structure gradually plays a supporting role, and the stress rebounds slowly. After the stress rebounds to the residual support strength, the spalling blocks of the specimen increase, the upper concave surface is compressed and deepened, and the microcrack on the surface of the residual structure extends and expands from the surface to the inside, forming a main crack through the residual support structure, resulting in the transverse expansion of the residual support structure. The residual support structure is damaged into several large blocks and loses its bearing capacity. Under the action of the upper indenter, the large block continues to slip and stagger, and the rebound stress of the specimen decreases gradually (Figure 11b). To sum up, the compression failure of the residual support structure caused by the penetrating main crack is the main reason for the cemented specimen from the post-peak stress rebounding to the complete unloading.

4. Conclusions

The characteristics of the post-peak stress rebound in the process of cemented body compression failure are analyzed. The maximum rebound stress is about 0.4–0.8 of the compressive strength. When the curing age is not more than 7 d, the compressive strength and maximum rebound stress of the cemented body generally increase with the curing age. The stress–strain curve model is a cubic function in the post-peak stress rising section and a quadratic rational function in the descending section. With the increase in the compressive strength of the cemented body, its maximum rebound stress also increases, and its corresponding compressive strain generally decreases. The rebound stress increment of cement is positively correlated with the strain increment. According to the change characteristics of the supporting structure and failure morphology of the cemented body before and after the maximum rebound stress, it is concluded that the compressive failure of the residual supporting structure caused by the penetrating main crack is the main reason for the cemented body from the post-peak stress rebound to the complete unloading.

Author Contributions: K.Y. contributed to the conception of the study; X.Z., Z.W., J.Z. and X.Y. performed the experiment; X.H. contributed significantly to analysis and manuscript preparation; X.Z. performed the data analyses and wrote the manuscript. All authors have read and agreed to the published version of the manuscript.

Funding: This paper was supported by the Anhui Province University Graduate Research Project (YJS20210389), the National Program on Key Basic Research Project of China (2019YFC1904304), and the Research Project of Institute of Energy, Hefei Comprehensive National Science Center (21KZS217).

Data Availability Statement: The data used in this research have been properly cited and reported in the main text.

Conflicts of Interest: The authors declare no conflict of interest.

References

1. Zhang, J.X.; Li, M.; Taheri, A.; Zhang, W.Q.; Wu, Z.Y.; Song, W.J. Properties and Application of Backfill Materials in Coal Mines in China. *Minerals* **2019**, *9*, 53. [[CrossRef](#)]
2. Tang, Y.G.; Guo, X.; Xie, Q.; Finkelman, R.B.; Han, S.C.; Huan, B.B.; Pan, X. Petrological Characteristics and Trace Element Partitioning of Gasification Residues from Slagging Entrained-Flow Gasifiers in Ningdong, China. *Energy Fuels* **2018**, *32*, 3052–3067. [[CrossRef](#)]

3. Dalce, J.B.; Li, L.; Yang, P.Y. Experimental Study of Uniaxial Compressive Strength (UCS) Distribution of Hydraulic Backfill Associated with Segregation. *Minerals* **2019**, *9*, 147. [[CrossRef](#)]
4. Rybak, J.; Adigamov, A.; Kongar-Syuryun, C.; Khayrutdinov, M.; Tyulyaeva, Y. Renewable-Resource Technologies in Mining and Metallurgical Enterprises Providing Environmental Safety. *Minerals* **2021**, *11*, 1145. [[CrossRef](#)]
5. Wang, Y.; Lei, Y.X.; Wang, S.Y. Green Mining Efficiency and Improvement Countermeasures for China's Coal Mining Industry. *Front. Energy Res.* **2020**, *8*, 18. [[CrossRef](#)]
6. Nurmi, P.A. Green Mining—A Holistic Concept for Sustainable and Acceptable Mineral Production. *Ann. Geophys.* **2017**, *60*. [[CrossRef](#)]
7. Yang, K.; Zhao, X.; Wei, Z.; Zhang, J. Development overview of paste backfill technology in China's coal mines: A review. *Environ. Sci. Pollut. Res.* **2021**, *28*, 67957–67969. [[CrossRef](#)]
8. Xu, Y.; Ma, L.; Ngo, I.; Zhai, J. Continuous Extraction and Continuous Backfill Mining Method Using Carbon Dioxide Mineralized Filling Body to Preserve Shallow Water in Northwest China. *Energies* **2022**, *15*, 3614. [[CrossRef](#)]
9. Xu, Y.; Ma, L.; Ngo, I.; Wang, Y.; Zhai, J.; Hou, L. Prediction of the Adaptability of Using Continuous Extraction and Continuous Backfill Mining Method to Sequester CO₂—A Case Study. *Minerals* **2022**, *12*, 936. [[CrossRef](#)]
10. Xue, Y.-C.; Xu, T.; Wasantha, P.L.P.; Yang, T.-H.; Fu, T.-F. Dynamic disaster control of backfill mining under thick magmatic rock in one side goaf: A case study. *J. Central South Univ.* **2020**, *27*, 3103–3117. [[CrossRef](#)]
11. Belem, T.; Benzaazoua, M. Design and Application of Underground Mine Paste Backfill Technology. *Geotech. Geol. Eng.* **2008**, *26*, 147–174. [[CrossRef](#)]
12. Zhao, X.; Yang, K.; He, X.; Wei, Z.; Zhang, J. Study on proportioning experiment and performance of solid waste for underground backfilling. *Mater. Today Commun.* **2022**, *32*, 103863. [[CrossRef](#)]
13. Fall, M.; Belem, T.; Samb, S.; Benzaazoua, M. Experimental characterization of the stress–strain behaviour of cemented paste backfill in compression. *J. Mater. Sci.* **2007**, *42*, 3914–3922. [[CrossRef](#)]
14. Cavusoglu, I.; Yilmaz, E.; Yilmaz, A.O. Sodium silicate effect on setting properties, strength behavior and microstructure of cemented coal fly ash backfill. *Powder Technol.* **2021**, *384*, 17–28. [[CrossRef](#)]
15. Kongar-Syuryun, C.; Tyulyaeva, Y.; Khairutdinov, A.M.; Kowalik, T. Industrial waste in concrete mixtures for construction of underground structures and minerals extraction. *IOP Conf. Ser. Mater. Sci. Eng.* **2020**, *869*, 032004. [[CrossRef](#)]
16. Kongar-Syuryun, C.; Aleksakhin, A.; Khayrutdinov, A.; Tyulyaeva, Y. Research of rheological characteristics of the mixture as a way to create a new backfill material with specified characteristics. *Mater. Today Proc.* **2021**, *38*, 2052–2054. [[CrossRef](#)]
17. Zhao, K.; Huang, M.; Yan, Y.J.; Wan, W.L.; Ning, F.J.; Zhou, Y.; He, Z.W. Mechanical properties and synergistic deformation characteristics of tailings cemented filling assembled material body with different cement–tailings ratios. *Chin. J. Rock Mech. Eng.* **2021**, *40*, 2781–2789.
18. Wang, Y.; Xiao, Y.; Hou, Z.; Li, C.; Wei, X. In situ X-ray computed tomography (CT) investigation of crack damage evolution for cemented paste backfill with marble waste block admixture under uniaxial deformation. *Arab. J. Geosci.* **2020**, *13*, 1018. [[CrossRef](#)]
19. Li, Y.; He, G.; Yu, M. Experimental study on the compressive strength of the backfills from cemented waste rock with cement and loess. *Chin. J. Undergr. Space Eng.* **2013**, *9*, 113–118.
20. Guo, Y.; Ran, H.; Feng, G.; Du, X.; Zhao, Y.; Xie, W. Deformation and instability properties of cemented gangue backfill column under step-by-step load in constructional backfill mining. *Environ. Sci. Pollut. Res.* **2022**, *29*, 2325–2341. [[CrossRef](#)]
21. Wu, J.Y.; Feng, M.M.; Yu, B.Y.; Chen, Z.Q.; Mao, X.B.; Han, G.S. Experimental study of strength and deformation characteristics of cemented waste rock backfills with continuous gradation. *Rock Soil Mech.* **2017**, *38*, 101–108.
22. Wang, J.; Fu, J.; Song, W.; Zhang, Y.; Wu, S. Acoustic emission characteristics and damage evolution process of layered cemented tailings backfill under uniaxial compression. *Constr. Build. Mater.* **2021**, *295*, 123663. [[CrossRef](#)]
23. Tu, B.; Liu, L.; Cheng, K.; Zhang, B.; Zhao, Y.; Yang, Q.; Song, K. A Constitutive Model for Cemented Tailings Backfill Under Uniaxial Compression. *Front. Phys.* **2020**, *8*, 173. [[CrossRef](#)]
24. Yang, L.; Xu, W.; Yilmaz, E.; Wang, Q.; Qiu, J. A combined experimental and numerical study on the triaxial and dynamic compression behavior of cemented tailings backfill. *Eng. Struct.* **2020**, *219*, 110957. [[CrossRef](#)]
25. Ermolovich, E.A.; Ivannikov, A.L.; Khayrutdinov, M.M.; Kongar-Syuryun, C.B.; Tyulyaeva, Y.S. Creation of a Nanomodified Backfill Based on the Waste from Enrichment of Water-Soluble Ores. *Materials* **2022**, *15*, 3689. [[CrossRef](#)]
26. Zhang, J.; Yang, K.; He, X.; Wei, Z.; Zhao, X.; Fang, J. Experimental Study on Strength Development and Engineering Performance of Coal-Based Solid Waste Paste Filling Material. *Metals* **2022**, *12*, 1155. [[CrossRef](#)]
27. Zhao, Y.; Soltani, A.; Taheri, A.; Karakus, M.; Deng, A. Application of Slag-Cement and Fly Ash for Strength Development in Cemented Paste Backfills. *Minerals* **2019**, *9*, 22. [[CrossRef](#)]
28. Tana, A.B.; Yin, S.; Wang, L. Investigation on Mechanical Characteristics and Microstructure of Cemented Whole Tailings Backfill. *Minerals* **2021**, *11*, 592. [[CrossRef](#)]
29. Lu, X.; Zhou, W.; Ding, X.; Shi, X.; Luan, B.; Li, M. Ensemble Learning Regression for Estimating Unconfined Compressive Strength of Cemented Paste Backfill. *IEEE Access* **2019**, *7*, 72125–72133. [[CrossRef](#)]
30. Li, M.; Zhang, J.; Li, A.; Zhou, N. Reutilization of coal gangue and fly ash as underground backfill materials for surface subsidence control. *J. Clean. Prod.* **2020**, *254*, 120113. [[CrossRef](#)]

31. Wang, Y.; Huang, Y.; Hao, Y. Experimental Study and Application of Rheological Properties of Coal Gangue-Fly Ash Backfill Slurry. *Processes* **2020**, *8*, 284. [[CrossRef](#)]
32. Zhang, X.; Lin, J.; Liu, J.; Li, F.; Pang, Z. Investigation of Hydraulic-Mechanical Properties of Paste Backfill Containing Coal Gangue-Fly Ash and Its Application in an Underground Coal Mine. *Energies* **2017**, *10*, 1309. [[CrossRef](#)]
33. Xiu, Z.; Wang, S.; Ji, Y.; Wang, F.; Ren, F.; Nguyen, V.-T. Loading rate effect on the uniaxial compressive strength (UCS) behavior of cemented paste backfill (CPB). *Constr. Build. Mater.* **2021**, *271*, 121526. [[CrossRef](#)]

Disclaimer/Publisher's Note: The statements, opinions and data contained in all publications are solely those of the individual author(s) and contributor(s) and not of MDPI and/or the editor(s). MDPI and/or the editor(s) disclaim responsibility for any injury to people or property resulting from any ideas, methods, instructions or products referred to in the content.